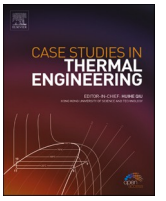
Case Studies in Thermal Engineering 66 (2025) 105714



Contents lists available at ScienceDirect

Case Studies in Thermal Engineering

journal homepage: www.elsevier.com/locate/csite





Structural optimization of solar chimney system based on heat efficiency and flow velocity: Numerical and Experimental studies

Jing Jia [a], Jing Nie [a,b,*], Hao Su [a], Jin-Chen XU [a], Xinyao Ruan [c], Wei Gao [d]

[a] College of Energy and Power Engineering, Inner Mongolia University of Technology, Hohhot, 010051, China
[b] Inner Mongolia Key Laboratory of Renewable Energy, Hohhot, 010051, China
[c] High School Affiliated to Inner Mongolia Normal University, China
[d] Huaneng Urad Middle Banner New Energy Generation Co., Ltd, China

ARTICLE INFO

Handling Editor: Huihe Qiu

Keywords:
Solar chimney system
Efficiency
Structural optimization
Thermal energy

ABSTRACT

This study focuses on enhancing the heat collection performance of solar chimney systems (SCS). The effect of various sizing parameters on the square SCS with a single side inlet is investigated through experimental and numerical simulations for optimization. The experimental results demonstrate significant variation in temperature uniformity among absorbers made from different materials. The composite absorber consisting of bamboo glue board, aluminum, sand, and black high-density polyethylene foam board exhibits excellent temperature uniformity. Optimization is performed with heat collection efficiency and chimney inlet fluid velocity as objective functions. The results indicate that adjusting the transparent cover inclination angle and chimney dispersion angle significantly enhances heat collection efficiency. Specifically, the SCS achieves a heat collection efficiency of 42.54 % when the inclination angle is set to 10° and the chimney dispersion angle is set to 1°. The chimney inlet fluid velocity of the SCS varies with different chimney dispersion angles at the same transparent cover inclination. At a dispersion angle of 2°, the velocity reaches a maximum of 2.090 m/s. Due to the large transparent cover area of the SCS, it is recommended to integrate the SCS with buildings and agriculture to achieve zero energy consumption and promote sustainable agriculture.

1. Introduction

In the context of global climate change, solar energy utilization technologies play an important role in helping to reduce carbon emissions. Solar energy technology reduces reliance on fossil fuels by utilizing solar energy to generate electricity and heat, resulting in lower greenhouse gas emissions. Solar chimney system (SCS) is one kind of environmentally friendly solar energy utilization technology. It can convert solar energy into internal air energy, then internal energy into kinetic energy, and finally into electrical energy. The research and application of the SCS can improve the efficiency of energy use and promote the development of new energy technologies. The concept of the SCS was proposed as early as 1903 and gradually attracted the interest of researchers in the following decades. It was not until 1978, when Schlaich [1] founded an entity in Germany and successfully operated it, that it attracted the extensive attention of researchers.

The SCS integrates the effects of a greenhouse, chimney, and turbine to facilitate heat and mass transport processes within the

* Corresponding author. College of Energy and Power Engineering, Inner Mongolia University of Technology, Hohhot. 010051, China.
E-mail address: n.j502@163.com (J. Nie).

https://doi.org/10.1016/j.csite.2024.105714
Received 13 October 2024; Received in revised form 20 December 2024; Accepted 28 December 2024
Available online 1 January 2025
2214-157X/© 2025 The Authors. Published by Elsevier Ltd. This is an open access article under the CC BY-NC-ND license (http://creativecommons.org/licenses/by-nc-nd/4.0/).

system [2]. The SCS has the advantages of pure energy and simple construction principles. The commercial application of the SCS has not yet been materialized due to the instability of solar radiation, nighttime discontinuities, and inadequate heat collection capacity. Recently, research on SCS has shifted towards structural optimization and integrated feature analysis, resulting in improved efficiency. Simple laboratory environments cannot accurately predict the performance of the SCS in natural settings. Therefore, some researchers have established outdoor SCS experimental systems to investigate their performance. A miniature outdoor experimental setup for the SCS is designed to evaluate its performance parameters [3]. The study found that different structural parameters affect the SCS, with the highest uniformity in the absorber temperature and the Gr number at the outlet of the transparent cover achieved with a 10° inclination angle of the cover [4]. The researchers work on optimizing the components of the internal SCS experimentation setup. The results show that different geometries affect the system's performance. For example, adjusting the chimney structure has a specific impact. It can improve the fluid velocity at the chimney inlet. Similarly, altering the geometry of the transparent cover brings another benefit. Furthermore, modifying the physical parameters of the absorber plays a role too. It boosts the absorber's capacity. Additionally, evolving the turbine mechanism also contributes positively. It improves the electrical performance of the system. These studies are less concerned with the relevant component interactions and the matching of the optimum values of the different parts of the structure. Therefore, this paper proposes to carry out a fitness study of the various structures of the SCS to select the appropriate structure and geometry.

The experimental study can directly allow people to observe the actual operation of the SCS and monitor the performance parameters such as internal temperature field, velocity field, and mass flow rate. During the experimental study, several key findings emerge. It is discovered that the environmental parameters of experimental weather are unpredictable and uncontrollable. This unpredictability has a significant impact on the results. Specifically, the ambient crosswind has a notable effect on the internal temperature field of the SCS. This crosswind also influenced the fluid velocity at the chimney inlet, as noted in Ref. [5]. However, it is impossible to directly observe the vortex motion inside the system due to the influence of the environmental conditions and the limitations of the experimental equipment. Considering these challenges, the researchers proposed a complex solution and suggested utilizing computational fluid dynamics software, which is capable of simulating and monitoring the effects of environmental crosswinds on the system. By creating an air domain within the simulation, researchers can observe how ambient crosswinds behave. Importantly, these crosswinds have been found to increase heat loss inside the system. Consequently, crosswinds contribute to a reduction in the thermal efficiency of the system, as reported in Ref. [6]. Addressing the impact of ambient crosswinds on the SCS is crucial. This paper introduces a targeted approach to mitigate this effect. It proposes reducing the windward surface area of the system, and it advocates designing the inlet as a single-side inlet. These design changes aim to achieve thermal insulation for the system. By implementing these strategies, the overall thermal efficiency of the SCS can be significantly improved.

Understanding the flow dynamics inside the SCS is essential. The primary flow mode within the system is natural convection. When airflow enters the interior of the SCS, an important observation can be made that the energy of the fluid at this point is insufficient to maintain its flow from the inlet to the outlet. This phenomenon, known as fluid reflux, occurs, and this reflux is characterized as a secondary flow within the system. The behavior of the secondary flow within the system deserves careful attention. This flow will naturally move from regions of high energy to those of low energy. Such movement has significant implications for the fluid dynamics within the SCS. It can exert an obstructive influence on the fluid flow in other parts of the system. This obstruction can disrupt the fluid flow and compromise the stability of the flow field within the SCS. The importance of the geometrical characteristics of the transparent cover in the SCS design has been highlighted by several researchers. These characteristics play a crucial role in heat transfer and fluid flow within the internal flow field of the SCS, as noted in Ref. [7]. To address certain challenges, researchers have proposed a specific design modification and suggested altering the structure of the transparent cover to a rectangular shape. This change, as reported in Ref. [8], has the potential to mitigate the negative effects associated with secondary flow. The SCS experimental setup has been modified to minimize heat loss and increase power output [9]. While increasing the diffusion angle of the chimney affects swirl and recirculation [10], increasing the inclination of the transparent cover and changing the radius of the transparent cover affects system performance [11]. When the radius of the transparent cover reaches a critical value, its contribution to the overall system is no longer significant [12]. The effect of heat storage materials on the heat collection performance of the SCS can be analyzed to select suitable materials that meet the heat storage requirements [13]. Currently, there is a notable gap in research regarding the comprehensive analysis of various factors affecting SCS performance. There is a lack of studies that simultaneously consider the dispersion angle of the chimney, the inclination angle of the transparent cover, and the absorber materials through both experimental and numerical simulations. To address this issue, this paper aims to contribute by filling this research gap. By providing detailed insights, it offers valuable research ideas for improving the efficiency of the heat collection system.

To reduce the negative impact of secondary flow, it is proposed above that the circular transparent cover of the SCS be modified to a square transparent cover to achieve this purpose. The SCS exhibits superior heat collection capabilities and advantageous structural characteristics. These attributes can be leveraged in practical applications. The SCS can integrate more heat-consuming systems. The overall thermal efficiency of the equipment can be significantly improved. Researchers have also proposed the integration of the SCS with various system structures such as desalination [14], photovoltaic systems [15], as well as methane removal structures [16], and facility-based agricultural systems [17], demonstrating the good compatibility of the SCS. This paper also proposes the integration of the SCS with square transparent covers with facility agriculture, considering the possibility of integration with buildings.

A review and analysis of existing literature on the SCS studies has been conducted. Altering the shape of the transparent cover has a notable impact on the characteristics of the transparent cover. Similarly, modifying the geometry of the transparent cover inlet also significantly influences these characteristics. These changes, in turn, affect the stability of the field flow within the SCS. There are several limitations associated with the circular structure of the traditional SCSs. This structure is not easily integrated with other heat collection systems. The circumferential inlet is prone to interference from ambient crosswinds, as noted in Ref. [18]. The chimney can

obscure part of the transparent cover surface, as reported in Ref. [19]. To address these issues, an analysis of the flow field characteristics inside the device was conducted. Based on this analysis, the traditional SCS parameters are optimized and improved. A theoretical foundation is established for enhancing and comprehensively characterizing the SCS structure.

The focus of this paper is to assess the optimization and enhancement of the SCS parameters. This study employs two pivotal metrics: optimal transparency cover efficiency and chimney inlet velocity, which serve as objective functions for evaluation. Through this rigorous analysis, the paper furnishes a robust theoretical foundation for advancing the SCS structure and enhances the comprehensive characterization of the SCS. In the ongoing research, several crucial decisions are being made regarding the design and materials used in the SCS. Firstly, the SCS system is designed, and preparations are made to build the experimental system. Secondly, the transparent glass cover material and appropriate heat storage material are carefully selected as the absorber. In addition, various materials and mounting methods for the absorber are being explored. Thirdly, the transparent cover design is optimized, especially considering different angles. Finally, numerical simulation studies are conducted on the SCS obtained from the above designs. Based on the study's results, a rectangular transparent cover closed on three sides is finally selected, aiming to minimize the effect of secondary flow and reduce heat loss.

2. Methodology

2.1. Operating principle

The traditional SCS inlet method is a round type. If the ambiance crosswind is violent, it penetrates the entire system. This penetration results in heat loss from within the system, thereby reducing its efficiency. Researchers have demonstrated that when solar radiation traverses the atmosphere and reaches the surface of the transparent cover, it initially heats the internal air and absorber. Additionally, the thermal response of the transparent cover is relatively slower. When fluid enters the SCS, it acquires energy through heat exchange. Some of this fluid comes into close contact with the inner surface of the transparent cover. Heat is lost from this fluid. This leads to idling and dissipation before the fluid reaches the chimney position. The circulation of the mainstream fluid, which is directed towards the chimney, is impeded. The energy of the fluid is weakened. This fluid is defined as secondary flow, which has the following main negative effects: 1) Increased heat loss from the transparent cover. 2) Instability of the flow field at the inlet of system. 3) Turbulent flow inside system. 4) Weakened the energy of the fluid at the inlet of the chimney. 5) Increased frictional resistance of the internal fluid.

Secondary flow has many negative effects on the SCS; therefore, this paper optimizes the SCS to reduce these effects. When developing new systems, this research considers the possibility of integrating them with agricultural cultivation to achieve synergistic development of multi-energy systems. Based on the structure of the local agricultural facilities, it is proposed to modify the transparent cover to achieve the purpose of matching each other. Therefore, the transparent cover is designed as a rectangle, which has been shown to reduce the negative impact of secondary flow, demonstrating the feasibility of this approach. To reduce the effect of ambient crosswinds, the round type of inlet is replaced by a single-side inlet, and the remaining three sides are designed as insulated walls. The use of a single-side inlet SCS increases the heat transfer efficiency of the system by preventing the overflow of hot fluid and reducing eddy currents at the junction of the side and back walls. The chimney location is also moved from the inlet to the north side, considering the sunlight angle, with the chimney adjacent to the rear side wall. The SCS is oriented towards the south side. This orientation aims to mitigate the negative impact of chimney shading on system performance. Additionally, it ensures that there is no shadow cast on the surface of the transparent cover during the peak radiation hours of the day. The SCS is divided into three parts: the chimney, the turbine, and the heat-collecting system, which consists of a transparent cover and an absorber [20]. Fig. 1 of this paper shows the modified SCS. The transparent cover is the basic structure for optical heat transfer and the absorber is the key heat storage

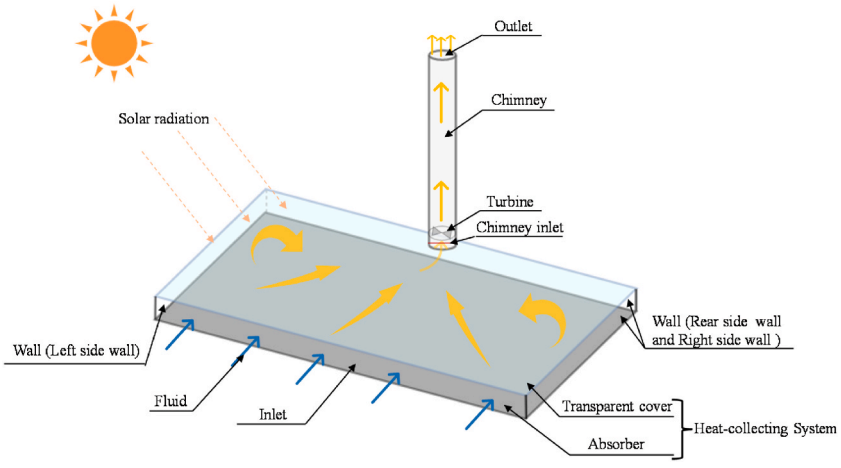


Fig. 1. Schematic diagram of the SCS.

component.

The air inlet has been modified to be single side to improve the heat transfer efficiency. The main purpose of this modification is to reduce energy loss and enhance heat transfer within the solar chimney system by optimizing the airflow path. (1) The air flow velocity changes significantly within the solar chimney system. Airflow enters the system through the inlet and is drawn into the chimney by the suction effect of the chimney. The large geometrical difference between the chimney diameter and the transparent cover creates a nozzle effect on the chimney inlet, amplifying the flow rate. The single-side air inlet design concentrates the airflow, increasing the temperature gradient inside the system and facilitating efficient thermal energy conversion. This configuration leads to an increase in airflow velocity at the chimney inlet. The increased velocity enhances the impact on the turbine blades, resulting in increased turbine output. (2) The single-side inlet configuration increases the temperature gradient within the system. As a result, the temperature of the airflow at the turbine inlet rises. A higher inlet temperature may lead to improved thermal energy conversion efficiency, potentially enhancing the turbine's overall efficiency. (3) The single-side inlet configuration may alter the distribution of flow resistance within the system. This change can reduce overall flow resistance and improve system efficiency. In summary, the single-side air inlet configuration impacts both heat transfer efficiency and turbine efficiency in the solar chimney system.

2.2. Experimental investigation

2.2.1. Experimental site

The experiment is conducted in Linhe District, which is in Bayannur City, Inner Mongolia Autonomous Region. Bayannur City is situated in the western part of the Inner Mongolia Autonomous Region. Specifically, Linhe District lies in the hinterland of the Hetao Plain. The experimental site falls within the longitude range of 107° 6′ to 107° 44′ and the latitude range of 40° 34′ to 44° 17′ [21]. The Linhe region has a temperate semi-arid continental climate. The average annual temperature is 6.8 °C. The average frost-free period is 127 days. The total annual radiation is about 6189.27 MJ/m^2. The number of hours of sunshine is 3254 h. Linhe District is a large agricultural city. The flourishing development of agriculture facilities is conducive to the combination of SCS and agricultural production, providing more favorable conditions for the comprehensive development of local multi-industry.

2.2.2. Experiment setup

According to the research conclusions of Golzardi et al. [16] and the similarity theory, the temperature field of the secondary flow SCS heat-collecting system is considered to reduce adverse effects. The shape of the transparent cover changes from a circular to rectangular aspect ratio of about 1:3. The transparent cover inlet is set with a unilateral rectangular channel, and the transparent cover surface area is about 2 m^2. Fig. 2 shows a schematic of the structure of the solar chimney system. Table 1 shows the dimensions of the SCS structure used in this paper. The transparent cover inclination angle as well as the chimney dispersion angle influence the transparent cover efficiency [22–28], so the parameter range of the SCS is chosen. The transparent cover inclination angle is 0°, 5°, 10°, 15° and 20°. The chimney divergence angle is 0°, 1°, 2°, and 3°. The inclination angle of the transparent cover influences the transparent cover outlet height.

The integral bracket of the SCS construction is made up of 4 cm × 4 cm angle steel, which is cut and polished by a grinding wheel. The height of the intake port at the bottom of the transparent cover bracket is adjustable. The upper and lower intake ports are supported by a combination structure consisting of a screw, spring, and universal wheel. The greenhouse's top is coated with glass that has an 85 % transmittance. This glass is 5 mm in thickness and exhibits excellent flame retardation properties. Additionally, it offers superior perspective and illumination transmission. The glass of the transparent cover and its holder are designed to be non-fastened, making them detachable. This feature facilitates easy construction and replacement, while also preventing adverse weather conditions from damaging the SCS experimentation system platform. The chimney is constructed of an aluminum plate with a thickness of 0.6 mm. The chimney is cylindrical with a diameter of 80 mm and a height of 1300 mm. The outlet section of the chimney (approximately 1/4 of the chimney's total height) is designed as a cylinder (the chimney divergence angle is 0°) and the round table type with distinct divergence angles (the chimney divergence angle is 1°, 2° and 3°). The four chimney configurations, as well as those for fixing the

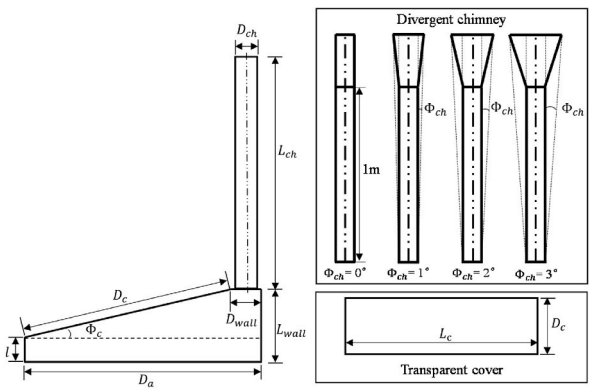


Fig. 2. Schematic diagram of the SCS.

Table 1
Structural dimensions of the SCS.

Structure	Value
Chimney height	1.3 m
Transparent cover inlet height	0.1 m
Chimney radius	0.04 m
Transparent cover area	2 m^2
Transparent cover inclination angle	0°, 5°, 10°, 15°and 20°
Chimney divergence angle	0°, 1°, 2°and 3°

chimney and adjusting the distance between the chimney and the ground, are shown in Fig. 3. Aluminum is selected as the metallic thermal conductive layer for the SCS absorber due to its density, thermal conductivity, and tensile reflection properties. Bamboo glue plates, sand, a dark film, and black high-density polyethylene foam plates are laid on the bottom of the entire system. The remaining three exterior wall materials are constructed from polystyrene foam board, which offers superior thermal insulation effects. Fig. 3 shows the layout of the adjustment structure applied to adjust the height of the transparent cover and the chimney. The sealant condition of the system is considered when the experimentation bed is built, and thick edges are set on three sides of the transparent cover to fit closely with the side walls.

2.2.3. Measurement and control system

As shown in Fig. 3, the SCS data acquisition system employs thermocouples for temperature measurement. These thermocouples measure the fluid temperature on the absorber surface, the inner transparent cover surface, the transparent cover inlet, and the chimney inlet. A thermocouple is arranged along the X direction on both the inner transparent cover surface and the absorber surface, enabling effective heat transport measurement. The KSE28B0R desktop multichannel temperature tester collects and outputs the temperature data. Anemometer 1 measures the velocity of the working fluid at the chimney inlet, while anemometer 2 is positioned outside the heat sink to monitor the ambient crosswind velocity.

The temperature field is monitored at specific temperature measurement points arranged within the SCS experimentation system. The arrangement of these temperature measurement points is depicted in Fig. 4. On the test platform, there are a total of 28 measurement points. The test platform is divided into two parts: the interior transparent cover surface and the absorber surface, together comprising 24 measurement points, as shown in Fig. 4(a). Additionally, one measuring point is positioned 10 cm from the chimney inlet, another is placed directly below the chimney's center on the absorber surface, and two more are arranged at the inlet of the transparent cover, as shown in Fig. 4(b). Each temperature test point is equipped with a PT100 adhesive platinum resistor, specifically type B. These resistors have a measurement range of −50 °C–200 °C and a precision of 0.1 °C. For collecting temperature field data, a PT100 adhesive platinum resistive temperature sensor and a KSE28B0R desktop multichannel temperature tester are used, with data collection occurring every 60 s. To measure the fluid velocity at the chimney inlet, an AS856S impeller high-precision split

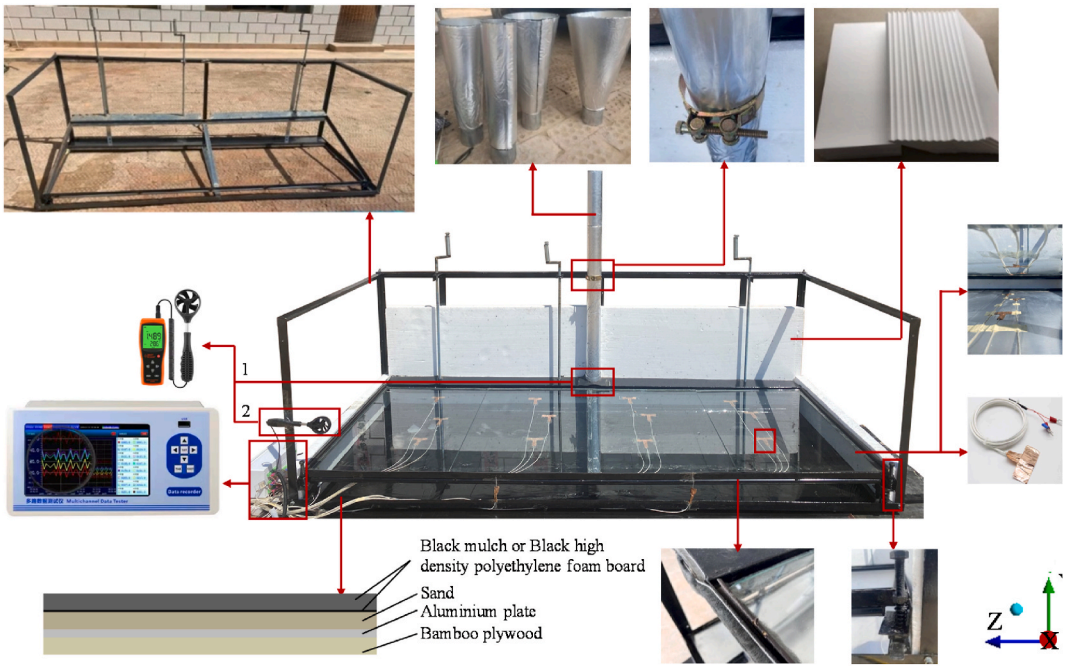
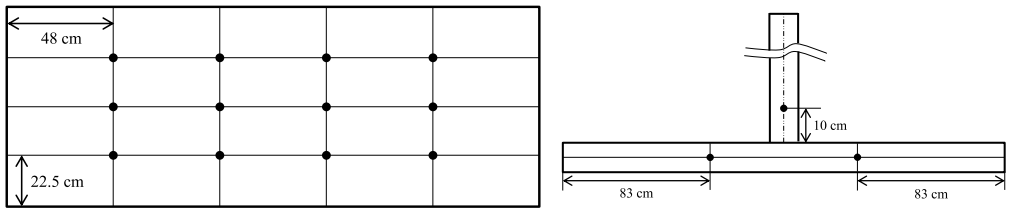


Fig. 3. An experimental bench and test apparatus for the SCS is developed in Bayan Nur City, China.



(a) Absorber and transparent cover. (b) Chimney inlet and transparent cover inlet.

Fig. 4. The SCS thermocouple measurement arrangement method.

anemometer is employed. This anemometer is connected to the laptop's USB interface for data storage and retrieval functions.

2.2.4. Uncertainty analysis

In the process of testing and measurement, the error generated by the measuring instrument will affect the accuracy of the test. This article selects fluid velocity, temperature, and other parameters for uncertainty analysis. Based on the principle of the statistical analysis method, equations (1) and (2) are applied to compute random uncertainty and system uncertainty [29].

$$\sigma_i = \sqrt{\frac{\sum_{i=1}^{n} (x_i - \overline{x})^2}{n-1}} \tag{1}$$

$$\mu_i = \frac{e_i}{\sqrt{3}} \tag{2}$$

Use equation (2) to combine random and system uncertainty [30].

$$u = \sqrt{\sum_{i=1}^{m_1} \sigma_i^2 + \sum_{i=1}^{m_2} \mu_i^2} \tag{3}$$

The uncertainty is computed using equations (1)–(3); the result is shown in Table 2.

2.3. Numerical simulation

2.3.1. Numerical model

The SCS experimental setup is detailed in Section 2.2 above. During testing, additional expenses are identified, including the cost of constructing the testbed, testing time, and workforce. Furthermore, it is found that internal turbulence within the system is not easily observable during testing. To address these limitations, numerical simulation is employed to complement the experimental work. Numerical simulation studies are conducted on the SCS testbed. The model size used in the numerical simulations matches the size of the experimental model. In experimental setups, various transparent cover inclination angles are selected for testing. However, the numerical simulation focuses solely on the SCS system with different chimney divergence angles, all under a fixed inclination angle of 10°, which corresponds to the desired inclination angle of the Spanish Manzanares the SCS prototype. The specific models studied include the 0° transparent cover inclination angle with 0° chimney divergence angle (0-0 SCS), the 10° transparent cover inclination angle with 0° chimney divergence angle (10-0 SCS), the 10° transparent cover inclination angle with 1° chimney divergence angle (10-1 SCS), the 10° transparent cover inclination angle with 2° chimney divergence angle (10-2 SCS), and the 10° transparent cover inclination angle with 3° chimney divergence angle (10-3 SCS).

2.3.2. Mathematical model

The SCS theoretical model is analyzed as follows. Firstly, it is assumed that the solar chimney system operates under steady-state flow conditions. Secondly, it is assumed that the internal air within the system behaves as an incompressible ideal gas. Furthermore, it is assumed that the temperature of the air entering the transparent cover remains constant. In the construction of the mathematical model in this paper, the following assumptions are made:

Table 2
Uncertainty of experimental parameters.

Parameters	Value/%
Temperature, K.	5.89
Velocity, m/s.	7.46
Heat collection efficiency, %.	6.83
Mass flow, kg/s.	3.51

(1) There is no heat source in the heat-collecting system.
(2) Assume that the state of the environment is stable.
(3) The buoyancy-driven flow is calculated using the Boussinesq approximation.

The simulation process is carried out by solving the steady state-governing equations by using the Finite Volume Method. This includes the continuity equation, momentum equation, energy equation [30], RNG K-ε model and DO radiation model.

Continuous equation:

$$\frac{\partial \rho}{\partial t} + \nabla \bullet \rho \vec{v} = 0 \tag{4}$$

Momentum conservation equation:

$$\nabla \bullet (\rho \vec{v} \vec{v}) = -\nabla p + \nabla \bullet \left(\mu \left[\left(\nabla \vec{v} + \nabla \vec{v}^{T} \right) - \frac{2}{3} \nabla \bullet \vec{v} \mathrm{I} \right] \right) + \rho \vec{g} \tag{5}$$

Energy conservation equation:

$$\nabla \cdot (\vec{v}(\rho E + p)) = \nabla \cdot \left(k_{eff} \nabla T - h_f \vec{j} + \left(\mu \left[(\nabla \vec{v} + \nabla \vec{v}^{T}) - \frac{2}{3} \nabla \cdot \vec{v} I \right] \cdot \vec{v} \right) \right) + S_h \tag{6}$$

The RNG K-ε model is used to describe the turbulent conditions in the computational domain [30]:

$$\frac{\partial (\rho k)}{\partial t} + \frac{\partial}{\partial x_i} (\rho k u_i) = \frac{\partial}{\partial x_j} \left[\left(\mu + \frac{\mu_t}{\sigma_k} \right) \frac{\partial k}{\partial x_j} \right] + G_k + G_b - \rho \varepsilon - Y_M + S_k \tag{7}$$

$$\frac{\partial (\rho \varepsilon)}{\partial t} + \frac{\partial}{\partial x_i} (\rho \varepsilon u_i) = \frac{\partial}{\partial x_j} \left[\left(\mu + \frac{\mu_t}{\sigma_\varepsilon} \right) \frac{\partial \varepsilon}{\partial x_j} \right] + C_{1\varepsilon} \frac{\varepsilon}{k} (G_k + C_{2\varepsilon} G_b) - C_{2\varepsilon} \rho \frac{\varepsilon^2}{k} - R_\varepsilon + S_\varepsilon \tag{8}$$

where G_k is the turbulent kinetic energy generated by the mean velocity gradient; G_b is the turbulent kinetic energy generated by the influence of buoyancy; Y_M is the influence of compressible turbulent pulsation expansion on the total dissipation rate; σ_k , σ_ε is the turbulent kinetic energy and the turbulent *Pr* number; $C_{1\varepsilon}$, $C_{2\varepsilon}$ is the dissipation rate, $C_{1\varepsilon} = 1.42$, $C_{2\varepsilon} = 1.68$.

DO radiation modeling is very general in solving the problem of internal radiative heat transfer in solar chimney systems [29,30], it converts the radiation transport equation into the transport equation for radiation in spatial coordinates (x, y, z), discretizes the radiation direction change, and solves the radiation transport equation covering the entire 4π space angles in the discrete direction. The radiative transfer equation for the absorbing, emitting, and scattering medium at position $\vec{r}$ in the direction of $\vec{s}$ is:

$$\nabla (I(\vec{r}, \vec{s}) \vec{s}) + (a + \sigma_s) I(\vec{r}, \vec{s}) = an^2 \frac{\sigma T^4}{\pi} + \frac{\sigma_s}{4\pi} \int_0^{4\pi} I(\vec{r}, \vec{s}') \Phi(\vec{s}, \vec{s}') d\Omega' \tag{9}$$

2.3.3. Boundary conditions

The 3D steady-state numerical simulations of the SCS with the boundary conditions depicted in Table 3 are performed using ANSYS finite component software. Experimental meteorological data for the Linhe District of Bayannur City are selected for the period from June to September. The ambient temperature of 300.15 K is taken as the mean value for the test site. The ambient crosswind velocity of 0 m/s is also considered the average for the test site. These values are utilized as the original boundary conditions for numerical simulation. For this reason, air property values near the ground are used in this research; the inlet and outlet pressures are atmospheric, and the ambient temperature is 300.15 K.

2.3.4. The verification of mesh independence

In this paper, the polyhedron mesh is used to mesh the SCS. For example, Fig. 5 is a 10-1 SCS meshing diagram with different models that utilize the identical method. The grids are 1, 2, 2.5, 3.5, 4, and 5.7 million to determine the independence of the results computed from the grid. The variation in the velocity and temperature of the chimney inlet fluid for different grid numbers is shown in Fig. 6, and the grid independence of the additional models is verified identically. If the grid size of the structure is large, the grid number is small, the calculation results are not accurate enough, and the deviation from the test is too large, there is no reference value. To some extent, the calculation accuracy can be increased by increasing the number of grids and decreasing the size of the mesh.

Table 3
Boundary conditions for the SCS.

	Boundary condition	Value
Inlet/Outlet	Pressure inlet/Pressure outlet	$\Delta P_0 = 0$ Pa, $T_0 = 300.15$ K.
Chimney	Wall (opaque)	Adiabatic; Wall thickness = 0.01 m.
Transparent cover	Wall (semi-transparent)	$h = 3.87$ W/m$^2 \cdot$K; Wall thickness = 0.007 m.
Absorber	Wall (opaque)	Constant heat flux; Wall thickness = 0.14 m.

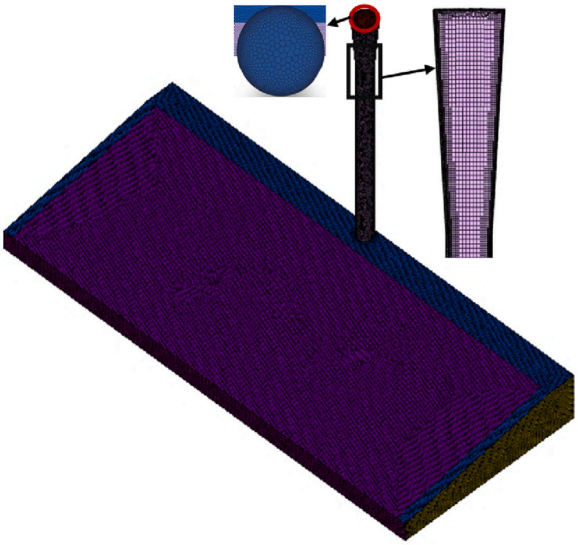


Fig. 5. Grid division model of 10-1 SCS.

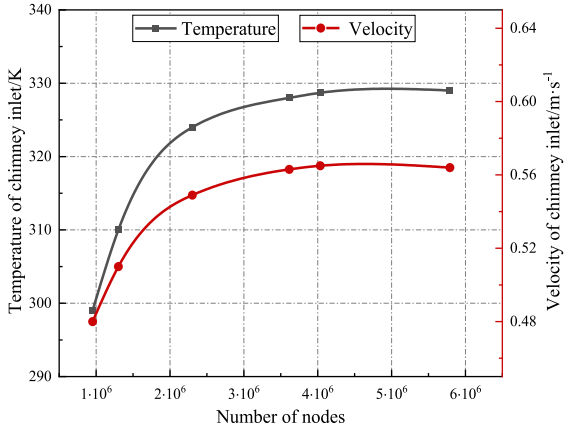


Fig. 6. Mesh independence verification based on chimney inlet velocity and temperature.

However, a vast mesh will also require additional computational resources that are not proportional to the increase in computational precision. In the SCS mesh partitioning, it has been found that an excessive number of meshes is generated during mesh reconstruction, which prolongs the computation time.

Several sets of calculations are conducted to verify the independence and representativeness of the data, as shown in Fig. 6. The number of grids significantly impacts the fluid temperature at the chimney inlet. Specifically, grid counts of 1 million, 2 million, and 2.5 million exhibit notable effects on the chimney inlet fluid temperature. However, grid numbers of 3.5 million, 4 million, and 5.7 million have a minimal influence on this temperature. The range of grid numbers varies from 1 million to 5.7 million, with a temperature variation percentage of 10 %. By comparing six different grid numbers, changes in fluid velocity at the chimney inlet can be observed. Specifically, after each increase in grid number, the fluid velocity changes by 6.35 %, 7.65 %, 2.55 %, 0.34 %, and 0.18 %, respectively. Notably, the amplitude of these changes decreases significantly after the third increase in grid numbers. Therefore, to save computing resources and reduce computing time without compromising calculation accuracy, 3.5 million grids are selected for the calculations.

2.3.5. The verification of numerical simulation

The experimental data from June to September are selected and compared with the simulation results of the SCS under the same boundary conditions. Temperature values are taken from the second thermocouple on the surface of the SCS absorber. These values are compared with the temperatures calculated by different numerical simulations, as illustrated in Fig. 7(a). The figure indicates that the

changing trend of the five SCS numerical simulation results aligns with the test values. The temperature difference between the data points is minimal, suggesting that the numerical simulation results are reliable. The numerical simulation method is precise, as evidenced by the consistency between the simulated and tested temperatures. The relative error of the calculation, which is determined by taking the mean value of the surface temperature from each SCS numerical simulation and comparing it with the test results in Fig. 7 (a), is presented in Table 4. The maximum error value is less than 2 %. This demonstrates that the numerical simulation method effectively predicts changes within the internal calculation domain.

The results of the 10-0 SCS test and numerical simulation at 13: 00 are compared with the results of Wang et al. [20] at the same time. The comparison results are shown in Fig. 7 (b). The results reveal that the relative error of the numerical simulation results is 0.2 %, and the relative error of the test results is 1.9 %. The comparison between experiment and simulation confirms the precise method used for the numerical simulation of the SCS. It ensures the selection of a more suitable computational method for the numerical simulation study during the calculation, which lays the theoretical foundation for the subsequent numerical simulation study of the SCS.

2.3.6. Analysis of error

The errors induced by the numerical simulation of the absorber surface temperature and the test data in Fig. 7 (a) above are analyzed as follows: 1) The error of the test data is generated by the error of the test instrument in the measurement process, and the test uncertainty is calculated in 2.3.4. 2) Artificial error: during the test, the experiment inlet is required to measure the operating parameters of the SCS in different periods, and there is a deviation between each measurement process and the last measurement process. 3) In this paper, the ray tracking model is used to compute the solar radiation value received by the SCS [31], ensuring that the carrying trend is consistent with that of the numerical simulation. Although the entire system is in a sunny area during the experimental measurements, the sidewalls will have created shades and projections onto the absorber surface because of the effect of the solar altitude angle, resulting in different absorption of solar radiation by the absorber. 4) The ambient temperature changes promptly during the test, which is not a wind-free condition, which affects the measured values of the SCS test; 5) The absorber framework in the test platform is made of angle steel welded and supported by 0.1m tall angle steel at the inlet, and the heat absorption rate of the steel is higher than that of rubber-plastic sponge material.

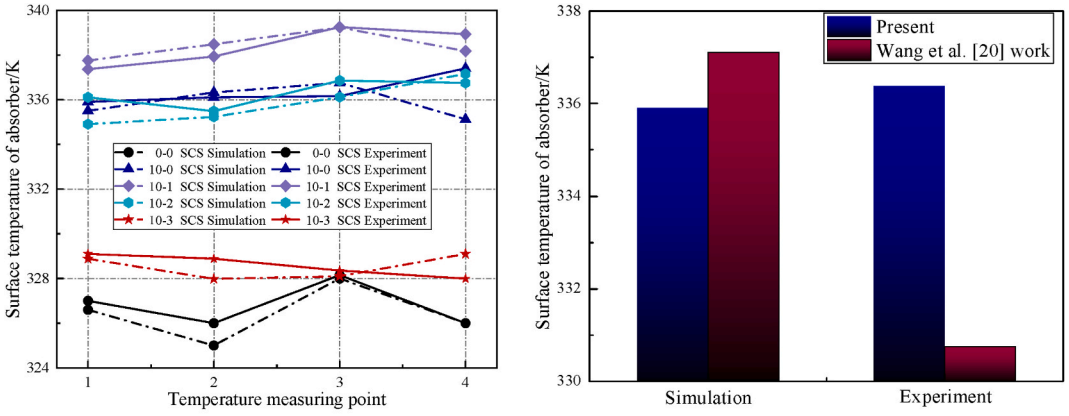
The errors generated by the numerical simulation and the experimental data of the absorber surface temperature in Fig. 7 (b) above are analyzed. The reasons for the mistakes are as follows: 1) During the numerical simulation, the absorber area of the model adopted by Wang et al. [20] is about six times that of the model used in this paper, so Wang et al. [20] can store more heat in the absence of ambient crosswind. 2) During the test, the position of the test bench of Wang et al. [20] is different from that constructed in this paper. Hohhot has a continental climate characteristic of the Mongolian plateau. Linhe district, on the other hand, features a semi-temperate and semi-arid continental climate. Hohhot is situated near the Yinshan Mountains. Due to its proximity to these mountains, the winds in Hohhot are stronger. Ambient crosswinds affect the SCS, and heat loss is significant. 3) The model used in this paper is the unilateral inlet, and the other three sides are made of thermal insulation material, so the test result of this paper is higher than that of Wang et al. [20]. The errors between the calculated values of the computational trials and the numerical simulations are less than 5 %, and the results are valid within reasonable mistakes.

3. Results and discussion

3.1. Experimental data analysis

3.1.1. Meteorological data analysis

Experimental data are analyzed during the period from July to September. Measurements are taken from 7:30 to 18:30 on days with



(a) Test and simulation verification. (b) Compare results with others.

Fig. 7. Comparison of numerical simulation and experiment.

Table 4
Errors between numerical simulations and experimental results for the SCS.

Data source of absorber surface temperature	Error				
	0-0 SCS	10-0 SCS	10-1 SCS	10-2 SCS	10-3 SCS
$\frac{\text{Simulation} - \text{Experimental}}{\text{Experimental}}$	1.06 %	1.21 %	0.96 %	1.12 %	1.18 %

clear, cloudless weather. Fig. 8 illustrates the typical daily variations in environmental conditions. Comparisons with results from both domestic and international researchers indicate that several factors significantly impact the heat harvesting performance of the SCS. These factors include air temperature, relative humidity of the air, zonal wind velocity, and solar irradiance. Thus, changes in air temperature, air relative moisture, zonal wind velocity, and solar irradiance on an average day are analyzed. The trends in air temperature display a gradual rise in temperature before 12:00. The temperature remains stable between 13:00 and 17:00. It decreases after 17:00. The relative moisture of the air maintains a gradual downward trend, which is influenced by solar irradiance and air temperature. When the temperature reaches its maximum, the water molecules evaporate more rapidly, resulting in lower relative air moisture. The ambient crosswind velocity remains between 0 and 2 m/s, implying a zonal wind velocity, with negative values indicating the opposite direction. The solar irradiance is unimodal and reaches its maximum at 13:00.

3.1.2. Optimum selection of absorber structure

To analyze the influence of different absorber materials on the thermal characteristics of the SCS, the experimental measurement of the SCS with varying absorber materials is carried out. Fig. 9 shows the surface temperature carried by the SCS absorber with various regenerative materials from 07:00 to 18:00. The regenerative surface temperature is divided into three layers; one layer is 25 cm away from the greenhouse inlet, and each layer is separated by 25 cm.

When comparing the surface temperature changes of five types of SCS absorbers with varying thermal storage materials, a pattern emerges. As the distance from the chimney decreases, the surface temperature of the absorber increases. Among these absorbers, a specific configuration stands out. This configuration features an absorber surface composed of three layers: bamboo glue board, aluminum, and black film. The temperature recorded at the temperature measuring point on this surface is the highest. It is found that the heat absorption effect of the black membranes is perfect, and the thermal conductivity of the aluminum plate is better. As a result, the absorber temperature is too high, and the maximum temperature is close to the melting point of the dark film (melting point: 105 °C–115 °C). The black membranes cannot conceal the aluminum plate and cannot be used continuously. It is less economical and is not friendly to the environment. The temperature field of a regenerated layer made of bamboo plywood, aluminum, sand, and black high-density foam board exhibits greater uniformity and stability than those of four other types of regenerated layer materials. After 12:00 noon, temperature measuring points on the four-layer absorber surface indicate minimal temperature gradients. The absorber surface maintains a high-temperature level throughout. These results demonstrate that an alloy absorber composed of bamboo glue board, aluminum, sand, and black high-density polyethylene foam board possesses excellent absorber performance. This absorber can provide constant and continuous heat to the SCS system. When compared to the experimental results of Das et al. [31], the absorber surface temperature field shows a similar trend, confirming the reliability of the research findings presented in this paper.

Fig. 10 illustrates the temperature difference between the absorber surface directly beneath the center of the SCS chimney, utilizing various materials, and a temperature measuring point located 10 cm at the chimney inlet. Specifically, the SCS absorber material made of bamboo rubber sheet + aluminum + black membrane exhibits a higher temperature value. In contrast, the SCS absorber materials composed of bamboo rubber sheets with aluminum and bamboo rubber sheets with aluminum and sand show lower temperature values, with these differences being insignificant. The temperature of the SCS absorber using bamboo plywood + aluminum + black high-density polyethylene foam board is 13.2 % lower than that of the absorber made with bamboo plywood + aluminum + black

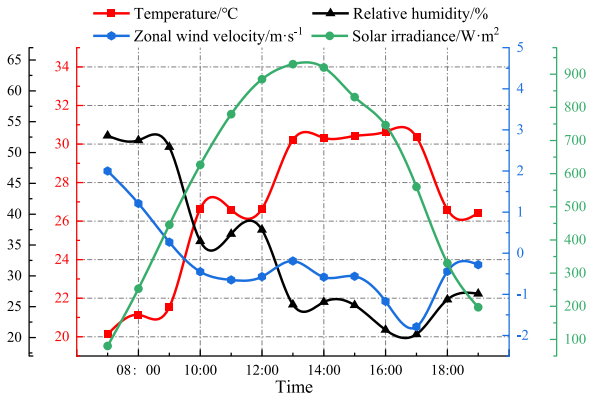


Fig. 8. The environmental parameters varied over time in the months of July and in August.

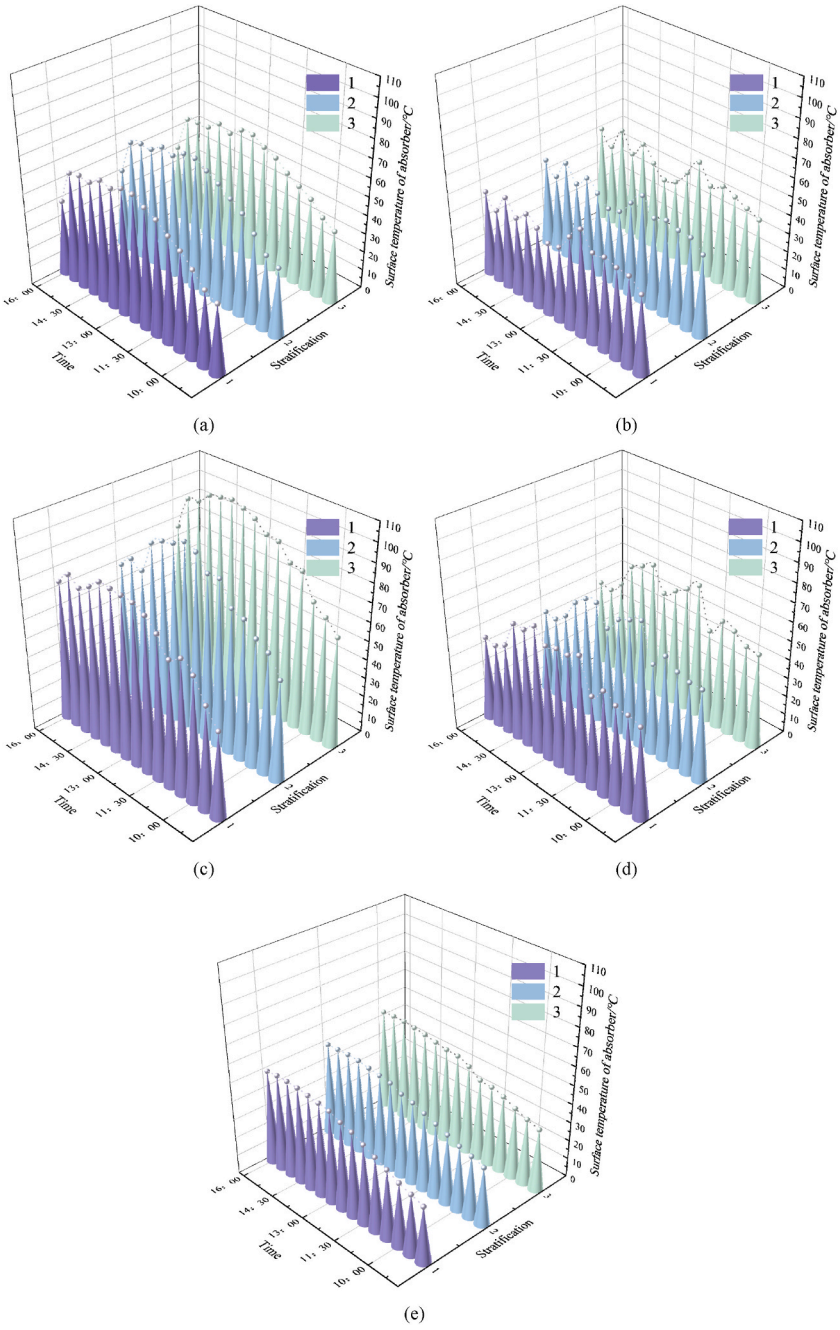


Fig. 9. Temperature profiles measured experimentally for different absorber materials: (a) Aluminum, (b) Bamboo glue board + aluminum, (c) Bamboo plank + aluminum + black membranes, (d) Bamboo plywood + aluminum + sand and (e) Bamboo glue board + aluminum + black high-density polyethylene foam board.

membrane. However, it is still higher than the temperatures of other materials. The temperature difference between the absorber surface directly below the chimney center, using bamboo plywood + aluminum + black high-density polyethylene foam board, and the temperature measuring point 10 cm away from the chimney inlet is moderate. When analyzing the changes in Figs. 9 and 10 together, it is evident that the absorber capacity of the bamboo glue board + aluminum + black high-density polyethylene foam board material is satisfactory. Additionally, the temperature field associated with this material is uniform and stable.

3.1.3. Optimum selection of transparent cover inclination angles

The absorber material is selected through 3.1.2. In this section, the absorber material is bamboo glue board + aluminum + black

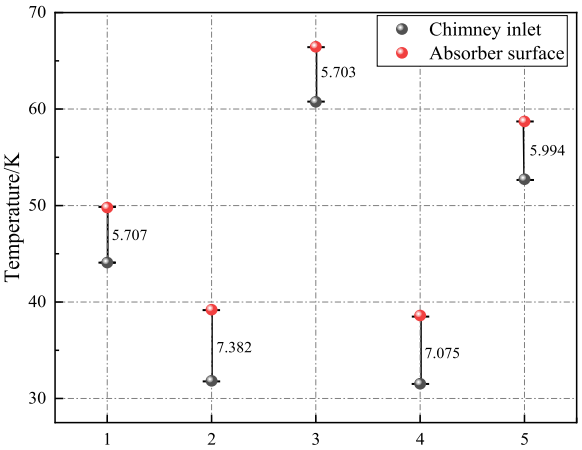


Fig. 10. The temperature difference between the chimney inlet and the absorber surface directly below the chimney: 1. Aluminum, 2. Bamboo glue board + aluminum, 3. Bamboo plank + aluminum + black membrane, 4. Bamboo plywood + aluminum + sand and 5. Bamboo glue board + aluminum + black high-density polyethylene foam board.

high-density polyethylene foam board. Fig. 11 shows the changes in the SCS absorber surface temperature with different transparent cover inclination angles from 07:30 to 18:30. The 0 scale is defined as 40 °C, and if the scale is more significant than zero, the temperature is greater than 40 °C, it is low. When comparing the variations in absorber surface temperatures across five different inclination angles of the greenhouse, a consistent pattern emerges. From 07:30 to 18:30, the absorber surface temperature initially rises and then decreases. Prior to 11:00, the surface temperature of all five SCS absorbers remains below 40 °C. After 11:00, the temperature consistently stays above 40 °C. Notably, when the inclination angle of the transparent cover is set at 10°, the absorber surface temperature is higher than that of the other systems. During the entire trial period, this temperature remains at a high level.

3.1.4. Optimum selection of chimney divergence angle

To minimize heat loss from the surrounding air and the transparent cover surface, temperature measuring points are strategically placed on the interior surface of the transparent cover. This surface is divided into three layers, with an equal distance between each layer. The average temperature fluctuations on the intermediate layer of the transparent cover surface are depicted in Fig. 12. Specifically, Fig. 12 (a) illustrates how the transparent cover surface temperature varies with a chimney divergence angle of 0°. From the diagram, it can be found that the temperature of the transparent cover surface is unimodal. At a chimney divergence angle of 0° and 3°, the transparent cover surface temperature is notably higher. The temperature change remains stable under these conditions. When the chimney divergence angle is set to 1° and 2°, the transparent cover surface temperature exhibits significant fluctuations. The temperature field becomes uneven under these circumstances.

Fig. 12 (b) shows the change in the temperature of the SCS transparent cover surface with different chimney divergence angles of 5°. The diagram indicates that the transparent cover surface temperature exhibits a unimodal pattern when the chimney divergence

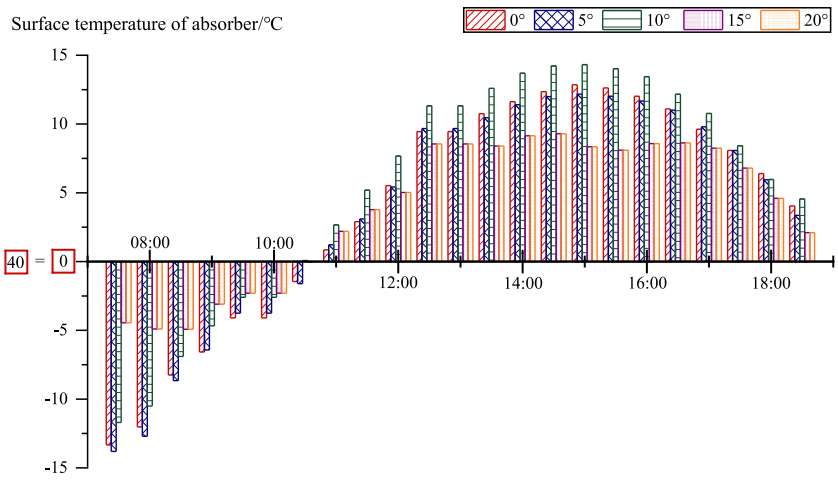
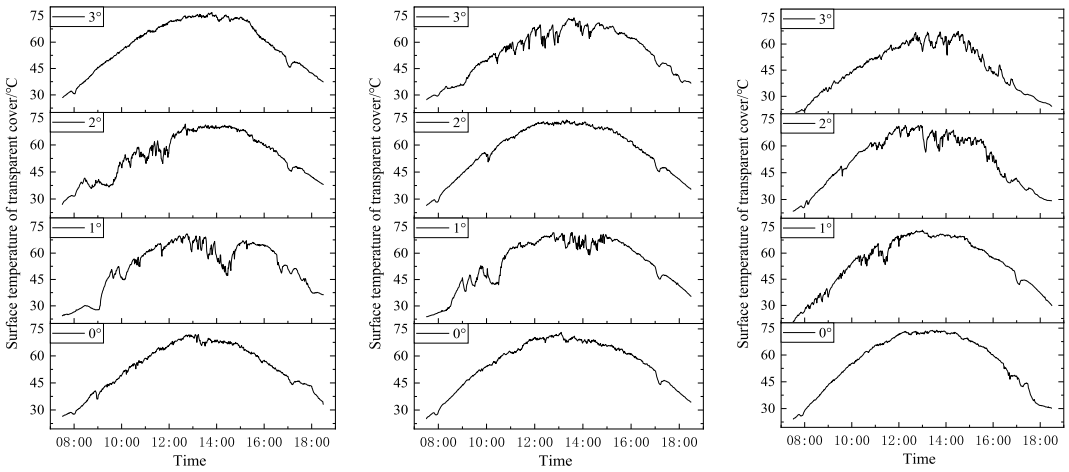


Fig. 11. Surface temperature variation of the SCS absorber at different transparent cover inclination angle.



(a) 0° inclination angle (b) 5° inclination angle (c) 10° inclination angle

Fig. 12. Surface temperature variation of the SCS absorbers at different chimney divergence angles.

angle is 0° and 2°, with peak temperatures occurring between 12:00 and 14:00. At chimney divergence angles of 1° and 3°, the transparent cover surface temperature fluctuates, resulting in a volatile system temperature field. Fig. 12(c) displays the changes in surface temperature for a 10° transparent cover with varying divergence angles of the SCS chimney. When comparing the trends among the four figures, it is evident that, at chimney divergence angles of 0° and 1°, the transparent cover surface temperature shows a distinct pattern, with minor differences in the maximum temperature values. Specifically, when the SCS chimney divergence angle is 1°, the temperature curve of the transparent cover surface declines gradually during the descending phase. At chimney divergence angles of 2° and 3°, the transparent cover surface temperature experiences fluctuations, and the temperature drops rapidly after 16:00.

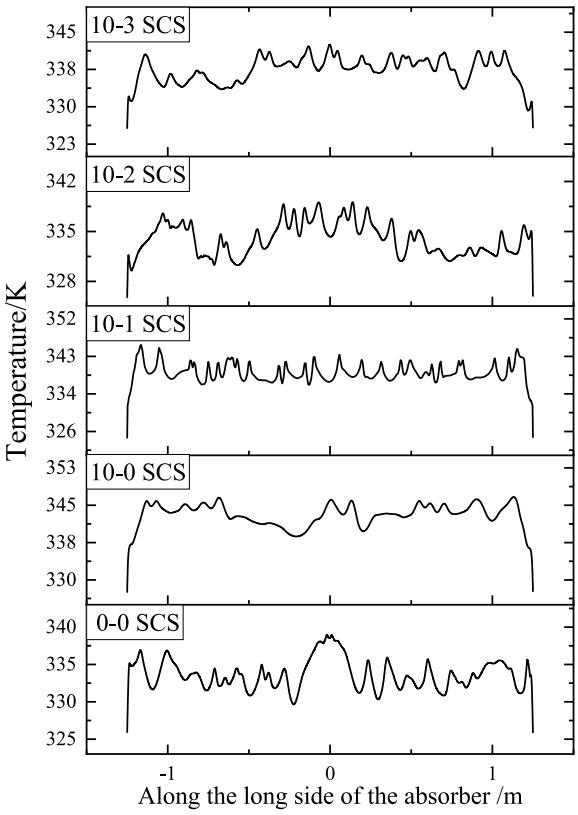


Fig. 13. Surface temperature variations for different SCS absorbers at 13:00.

Based on similarity theory, a test bench for the solar chimney system is set up in the Lin-he District of Bayannur City, Inner Mongolia, and the SCS test data is analyzed. The optimal inclination angle of the transparent cover is determined by optimizing various factors, including the angles of the SCS transparent cover, the chimney divergence angle, and the absorber material in the ring. Analysis of test data related to the temperature and velocity fields of the SCS transparent cover system leads to several conclusions. At a 10° inclination angle, the absorber temperature field demonstrates good uniformity. The fluid temperature field at the chimney inlet also shows favorable distribution characteristics at this angle. The stability of both the flow field and surface temperature field of the SCS transparent cover system is excellent at a 10° inclination angle. When the transparent cover inclination angle is set to 10°, the SCS with a 1° chimney divergence angle exhibits superior heat collection performance. However, the SCS test system has limitations in fully detecting the internal fluid temperature field, intensity distribution, and other relevant parameters. The system is unable to predict the fluid behavior within the SCS internal flow field after it passes through the chimney inlet section. A numerical simulation study of the SCS test system provides a solid foundation for future research.

3.2. Analysis of simulation results

3.2.1. Temperature field

To investigate the absorber characteristics of various materials, the effects of the angle of inclination of the transparent cover and the angle of dispersion of the chimney on the SCS absorber are analyzed. Absorber systems are selected to complement and validate the test conclusions. Fig. 13 depicts the surface temperature profile of the absorber located directly beneath the chimney for different SCS configurations, including 0-0 SCS, 10-0 SCS, 10-1 SCS, 10-2 SCS, and 10-3 SCS, all measured at 13:00. This figure directly illustrates the temperature variations on the SCS absorber surface. By comparing the surface temperature of the absorber, it is found that the temperature rises by about 3 % when the inclination of the transparent cover is changed from 0° to 10°. When the transparent cover inclination angle remains at 10° and the chimney divergence angle varies from 0° to 3°, the maximum absorber surface temperature decreases progressively. Among these configurations, the maximum temperature of the middle layer in the 10-0 SCS is notably the highest. Conversely, the temperature range in the 10-1 SCS is relatively narrow.

Fig. 14 displays a cloud map of the fluid temperature distribution at 13:00 in the symmetry planes of the 0-0 SCS, 10-0 SCS 10-1 SCS, 10-2 SCS, and 10-3 SCS. The temperature scale displays the maximum temperature of the Y-Z symmetric surface. When comparing the Y-Z symmetric surface fluid distribution cloud pictures of the five SCS configurations, the 10-0 SCS exhibits the highest fluid temperature. The cloud maps indicate that the higher temperature fluid is distributed across most of the 10-0 SCS system. The fluid temperatures on the Y-Z symmetric surface of the 10-1 SCS are also significant, but the higher temperature values are concentrated on the transparent cover surface. As this fluid is transported from the greenhouse to the absorber, it undergoes heat loss. Upon examining

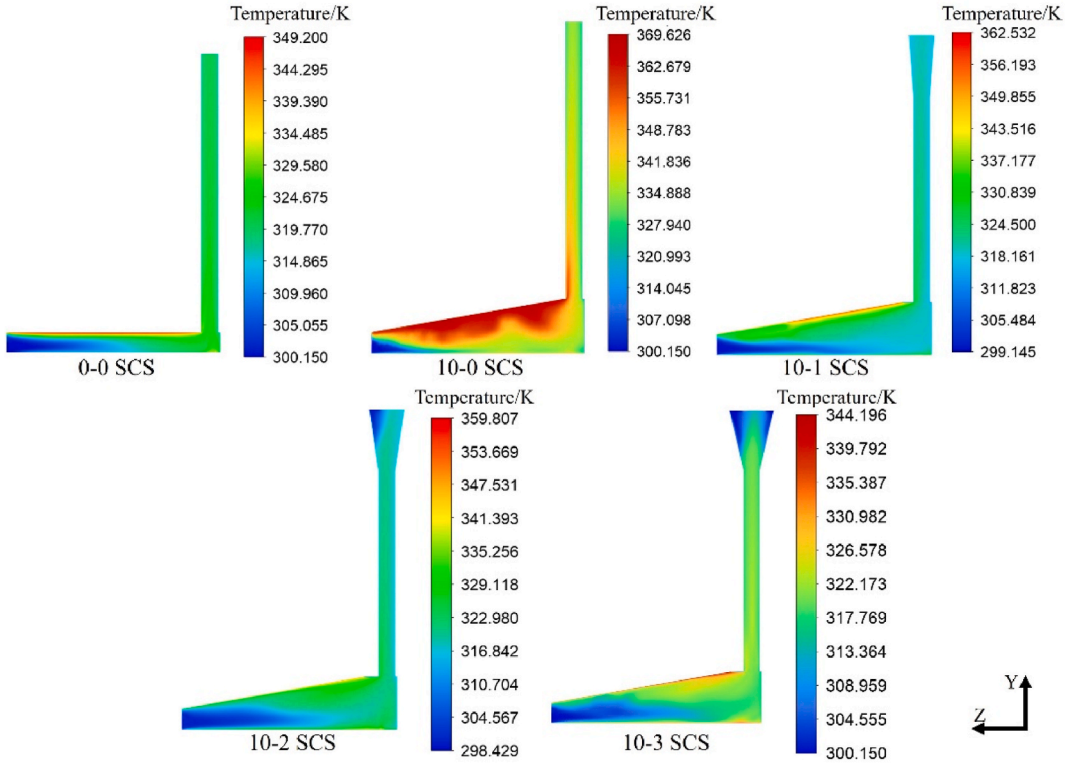


Fig. 14. Cloud-temperature maps of the Y-Z symmetry plane for different SCS at 13:00.

Fig. 14, it becomes evident that an increase in the transparent cover's inclination angle from 0° to 10° leads to an enlargement of the transparent cover outlet and an expansion of the system space below the chimney inlet. This expansion allows for the storage of more thermal fluid. The energy needed to facilitate smooth fluid flow from the chimney inlet to the outlet is also observed. Notably, at the transparent cover inlet of the 10-1 SCS, the fluid's pathway into the system is longer compared to that of the 10-0 SCS. As the inclination angle of the transparent cover in the 10-0 SCS increases, the volume of the cavity beneath it also expands.

When the inclination angle of the transparent cover remains constant, an increase in the chimney divergence angle enhances the chimney's suction effect. This leads to an increased path distance for the suction of cold air under the chimney. Consequently, the internal heat loss of the system rises. In both the 10-2 SCS and 10-3 SCS, a clearer backflow of ambient cold fluid into the SCS at the chimney outlet can be observed. Upon comparing the results of the above SCS numerical simulations of the temperature field with experimental data, it is found that the 10-1 SCS demonstrates superior absorber performance. Therefore, the 10-1 SCS serves as a reference for further optimization of solar chimney systems.

Fig. 15 displays the fluid temperature variation at the chimney inlet for different regimes from 07:30 to 18:30. The temperature value corresponding to the zero scale is 315 K. The figure shows that the initial temperature of the fluid in the 0-0 SCS is the highest. During continuous operation of the fluid system, the temperature at the 10-0 SCS chimney inlet increases rapidly. At noon, the highest temperature is observed at the 10-0 SCS chimney inlet, indicating that additional heat is present at the chimney inlet of the system. In this paper, the operation of the SCS under actual weather conditions at different times of the day is simulated using the DO radiation model and ray tracing model. These numerical simulation calculations mimic the solar radiation depicted in Fig. 8. Consequently, the solar irradiance and ambient temperature peak at 13:00. Simultaneously, the fluid temperature at the chimney inlet responds rapidly and attains its maximum value.

3.2.2. Velocity field

Fig. 16 shows the variation of the fluid velocity at the chimney inlet for different regimes from 07:30 to 18:30. Both pressure ingress and pressure egress boundary conditions are applied in numerical simulations, which do not possess an air domain and do not consider the effect of ambient crosswinds. The variation of the fluid velocity at the different SCS chimney inlets is compared, and it is found that the fluid velocity at the 10-2 SCS chimney inlet remains stable, with a maximum value close to 1.6 m/s. When compared to the fluid variation at the chimney inlet, it is observed that the maximum fluid velocity occurs at the chimney inlet of the SCS with a 2° chimney divergence angle at 12:30. This velocity is higher than that of other systems at the same time. The fluid velocity at the chimney inlet serves as a criterion for selecting the chimney divergence angle. The heat collection performance of the SCS is optimal when the chimney divergence angle is 2°. The movement trend of the fluid at the chimney inlet aligns with the findings of Praveen et al. [32]. Friction has a significant impact on the velocity of the fluid near the chimney wall.

Fig. 17 displays a cloud map of the fluid temperature change at the chimney inlet at 13:00 for various systems. During numerical simulations, the environment is set to be wind-free. The 0-0 SCS, 10-0 SCS, 10-1 SCS, 10-2 SCS, and 10-3 SCS are located along different sections along the chimney direction, ranging from the chimney inlet to the outlet. When compared to the other five solar chimney systems, the trend of fluid velocity changes along the symmetry axis of the chimney, specifically at the 3/4 point, is generally similar. The position where the fluid velocity peaks is not at the chimney inlet. Instead, the fluid velocity continues to increase before reaching the chimney inlet due to the nozzle effect. This effect causes the fluid to be influenced in such a way that most of the heat energy it carries is converted into kinetic energy. A small portion of the heat is lost due to frictional resistance. After reaching its maximum value, the fluid experiences a slight decrease in velocity, allowing it to maintain a consistent speed at the middle and end sections of the chimney.

The 0-0 SCS transparent cover outlet height is the same as its inlet height. Between 0 and 0.1 m (upon reaching the chimney inlet), the fluid velocity increases to approximately 1.3 m/s and remains above 1.25 m/s once inside the chimney. When the inclination angle of the transparent cover is adjusted, the outlet height of the transparent cover increases. For the 10-0 SCS, 10-1 SCS, 10-2 SCS, and 10-3 SCS, the outlet height is uniformly set at 0.256 m. The 10-0 SCS fluid exhibits a similar velocity change trend upon entering the chimney as the 0-0 SCS fluid. The maximum fluid velocity at the chimney inlet of the 10-0 SCS is 22.3 % higher than that of the 0-0 SCS.

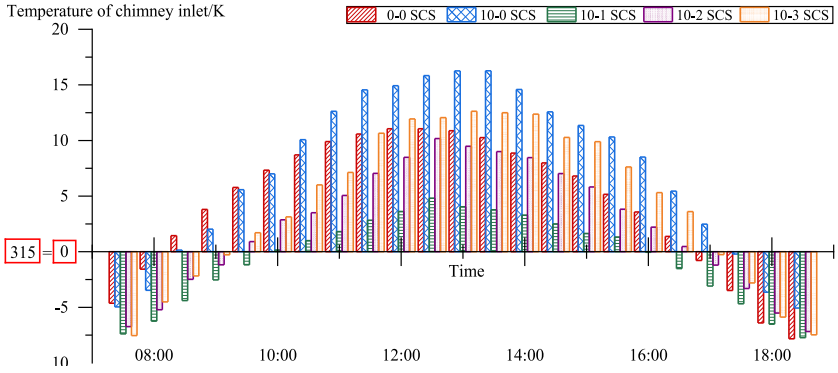


Fig. 15. Comparison of fluid temperatures at the chimney inlet for different SCS from 07:30 to 13:00.

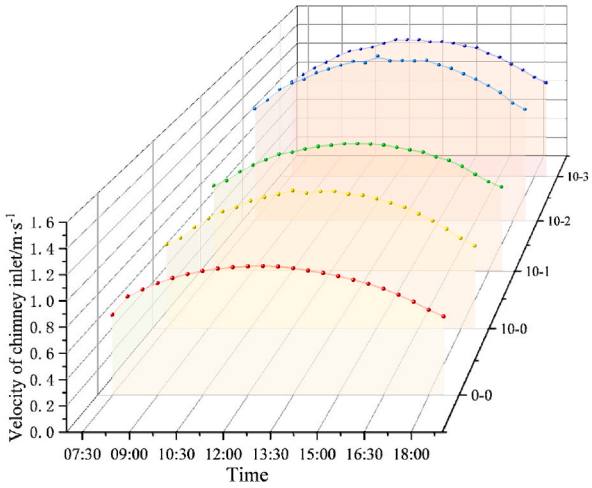


Fig. 16. Comparison of fluid velocity at the chimney inlet for different SCS between 07:30 and 18:30.

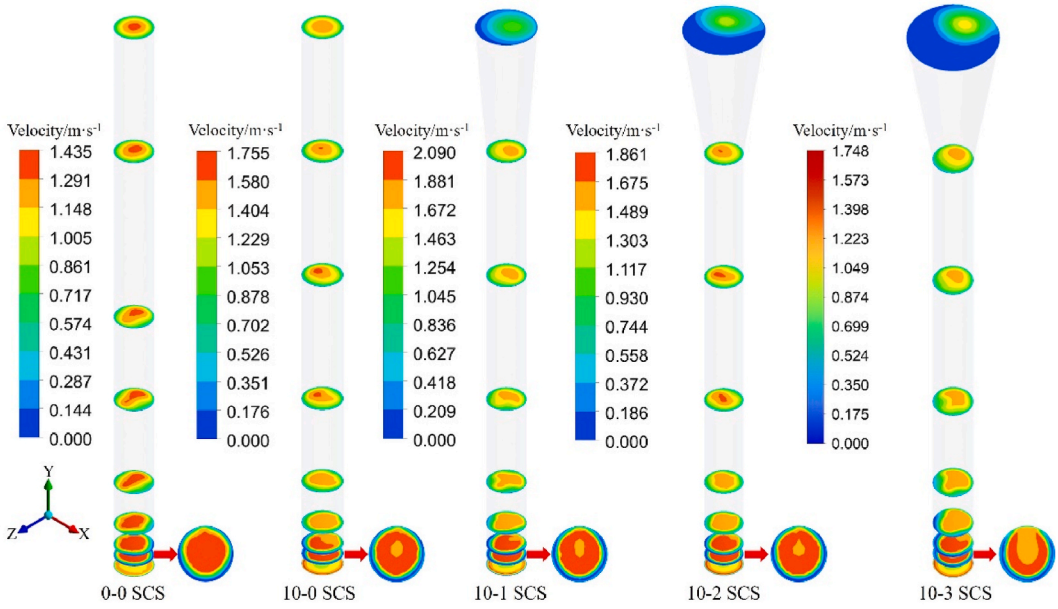


Fig. 17. Comparison of fluid velocity in different sections of the SCS chimney at 13:00.

The chimney divergence angles for the 10-1 SCS, 10-2 SCS, and 10-3 SCS are 1°, 2°, and 3°, respectively. Upon comparing the fluid velocity variations of these three systems in Fig. 17, it is found that the 10-1 SCS has the highest fluid velocity at the chimney inlet. As the divergence angle increases, the decrease in fluid velocity is less significant. The fluid velocity trend of the 10-2 SCS closely resembles that of the 10-1 SCS but with a lower maximum fluid velocity. The velocity field of the 10-3 SCS fluctuates, indicating poor stability.

3.2.3. Pressure field

The changes of hydrodynamic pressure on the chimney central axes of 0-0 SCS, 10-0 SCS, 10-1 SCS, 10-2 SCS, and 10-3 SCS from 07:30 to 18:30 are shown in Fig. 18. As the dynamic pressure on the absorber surface is 0 Pa and moves along the chimney's central axis towards the outlet, the hydrodynamic pressure of the five SCS systems initially rises, then decreases, and subsequently increases. Among these, the hydrodynamic pressure at the chimney inlet of the SCS with a 10° inclination angle transparent cover experiences the most significant variation. The pressure difference here serves as a crucial pressure guarantee for hot air to push the turbine blade and perform work. The divergence angle has a significant impact on the fluid pressure within the SCS chimney. Therefore, choosing the right design and configuration is essential for enhancing the performance of the SCS systems. Nasraoui et al. [33] have observed that the Venturi effect can account for the rapid acceleration of fluid at the chimney inlet. Furthermore, the pressure at the chimney inlet

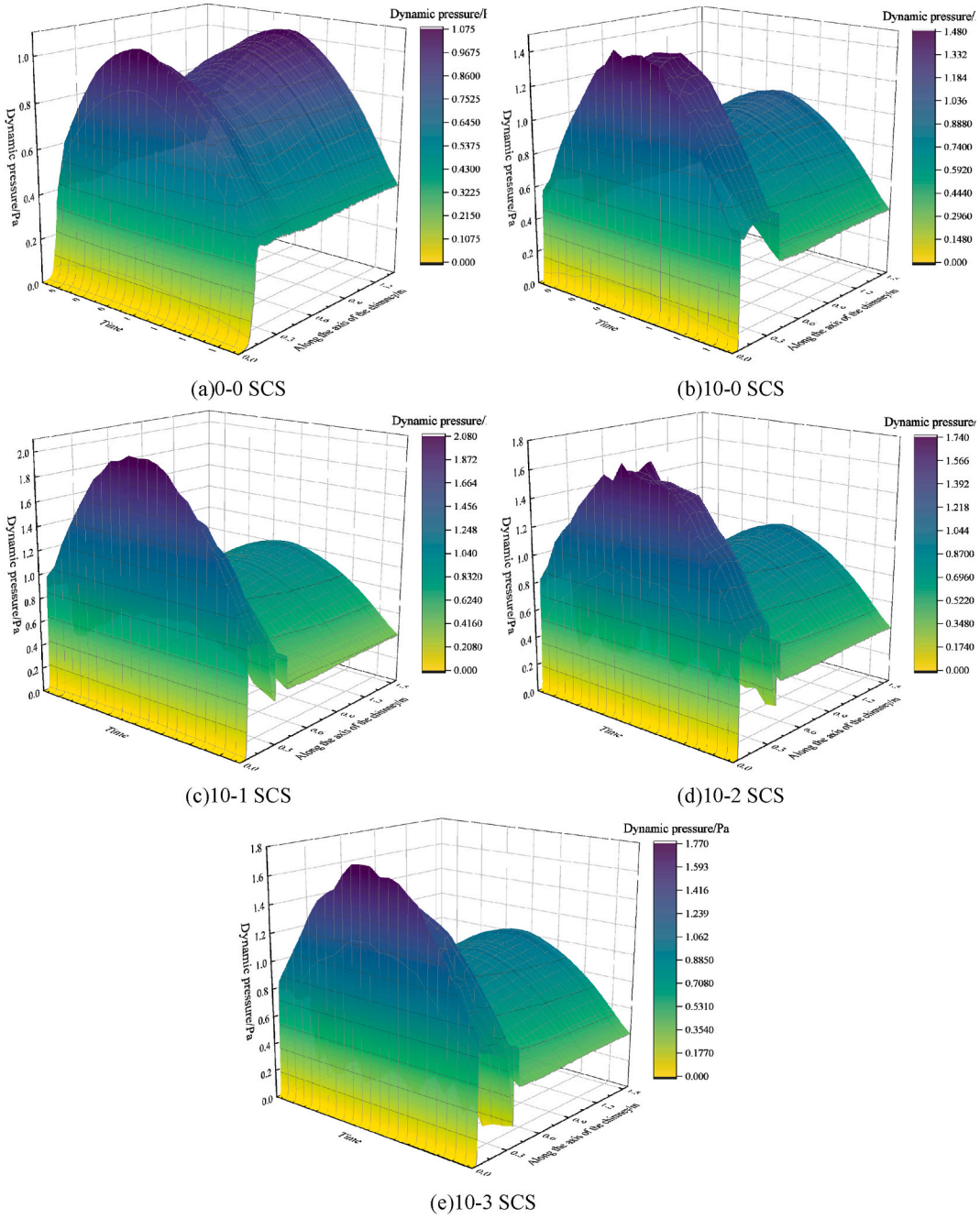


Fig. 18. Comparison of the hydrodynamic pressure on the chimney symmetry axis for different SCS from 08:00 to 13:00.

undergoes notable changes along the central axis of the chimney.

3.2.4. Nusselt Number

The Nusselt number (*Nu*) denotes the intensity of convective heat transfer [34], and the calculation formula is as follows:

$$Nu = \frac{hl}{k} \tag{10}$$

$$h = 3.87 + 0.0022\left(\frac{u_0 \rho_0 C_p}{pr^{\frac{2}{3}}}\right) \tag{11}$$

$$Pr = \frac{\mu Cp}{k} \tag{12}$$

where l is the characteristic length, m; k is the thermal conductivity of the fluid, W/m · K; h is the convective heat transfer coefficient of the fluid [41], W/m^2 · K, the calculation formula is (11); u_0 is the ambient crosswind velocity, m/s; μ is the fluid viscosity, Pa · s; C_p is the specific heat capacity, J/kg · K; Pr is the Prandtl number, the calculation formula is (12).

When the boundary conditions are determined in the numerical simulations, the transparent cover inlet is the pressure inlet, and the ambient temperature is 300.15 K. The interior fluid domain of the SCS is calculated, but the peripheral fluid is not selected, so the thermal conductivity of the fluid is chosen according to the boundary conditions. The relevant parameters for the fluid on the absorber surface the transparent cover surface, and the chimney outlet are given in Table 5. By calculating the local Nusselt numbers of the five SCS at 13:00, the Nusselt numbers of the five SCS transparent cover inlets are identical, all 15.09. The Nusselt numbers for the five absorber surfaces are 117.04, 115.95, 115.98, 116.96, and 117.12. The Nusselt numbers for the five transparent cover surfaces are 115.56, 111.74, 111.99, 112.25, and 112.07, respectively. The Nusselt numbers for the five chimney outlets are 12.21, 12.47, 18.21, 27.39, and 34.00, and the convective heat transfer coefficients for the five chimney outlets in the system are 4.30, 4.37, 4.26, 4.26, and 4.32. When the regional Nusselt numbers are at different locations, it is found that varying geometry affects the fluid velocity and temperature in the system, resulting in a natural improvement of the flow rate and a shift in the local Nusselt number.

3.2.5. Heat collection efficiency

The effectiveness of heat harvesting is the most influential assessment metric for heat harvesting performance. A suitable system is selected by comparing heat harvesting efficiency. The formulation of heat harvesting efficiency η is as follows:

$$\eta = \frac{\rho_{coll} v_{out} A_{ch} C_p \Delta T}{I A_{coll}} \tag{13}$$

Where ρ_{coll} is the air density at the opening temperature of the transparent cover, kg/m^3; v_{out} is the air velocity at the opening temperature of the transparent cover, m/s; A_{ch} is the cross-sectional area of chimney, $A_{ch} = \left(\pi D_{ch}^2\right)/4$, D_{ch} is the diameter of the chimney, m; C_p is the specific heat capacity, J/(Kg · K); ΔT is the difference between the opening temperature of the transparent cover and the ambient temperature, K; I is the intensity of solar radiation intensity, W/m^2; A_{coll} is the area of the transparent cover, m^2; A_{ch} is the cross-sectional area of the chimney, m^2.

The heat harvesting efficiencies of 0-0 SCS, 10-0 SCS, 10-1 SCS, 10-2 SCS, and 10-3 SCS are shown in Fig. 19. The heat collection efficacy of the above five SCS is calculated by formula (13). The heat harvesting efficiency of 0-0 SCS, 10-0 SCS, 10-1 SCS, 10-2 SCS, and 10-3 SCS is 22.21 %, 35.63 %, 42.54 %, 29.99 %, and 30.40 %, respectively. Compared to the heat collection efficiency of the SCS, it is found that when the inclination angle of the transparent cover is raised to 10°, the heat collection efficiency of the SCS increases by 60.42 %. In the analysis of the preceding sections of this chapter, it is concluded that the performance of the 10-1 SCS is excellent, with the most incredible warm harvesting effectiveness, 91.54 %, 19.00 %, 41.85 %, and 39.93 % higher than the 0-0 SCS, 10-0 SCS, 10-2 SCS and 10-3 SCS.

The increase in the inclination angle of the transparent cover increases the volume of the cavity below the transparent cover, enabling additional cold fluid to penetrate the SCS and more cold fluid to be stored in the SCS. The heat-harvesting efficiency of the SCS increases with the fluid volume flow rate and the temperature of the heat-harvesting system. Different chimney divergence angles and increased chimney effects affect the fluid inside the chimney, but expanding the chimney divergence angle harms the heat collection characteristics of the SCS. To some extent, the fluid pressure is reduced at the chimney outlet, allowing the ambient crosswind to inlet the chimney, directly leading to a reduction in the heat collection efficiency of the SCS.

4. Feasibility analysis of integration with other systems

The existence of secondary flows in the SCS system reduces the energy conversion rate. This negative impact is considered during the structural optimization process described in this paper. The important energy conversion structure is redesigned in this process. The development of local facility agriculture and the energy efficiency of urban buildings is considered. The zero-carbon emission solar chimney system works better when combined with both. As the global energy crisis intensifies, finding sustainable and environmentally friendly energy solutions becomes urgent. Combining SCS with agricultural greenhouses and sky gardens responds positively to this need. Urbanization accelerates, leading to a decrease in urban green space. This design approach saves energy, reduces emissions, and provides more green leisure space for urban residents. It also improves the quality of urban living. This integrated design allows for the development of efficient and sustainable agricultural greenhouses and sky garden systems. It offers new possibilities for modern agriculture and urban development [35].

4.1. Integration with agricultural greenhouses

SCSs integrate with agricultural greenhouses to create an innovative technology that combines renewable energy with modern agriculture. This integration aims to enhance energy efficiency and increase crop yields. SCS generates thermal energy by installing transparent materials on top of the greenhouse. These materials collect solar energy and heat the air, causing a natural convection current. The thermal energy provides necessary temperature regulation inside the greenhouse and can also be converted into

Table 5
Fluid-related parameters for heat sink, absorber, and outlet.

	Viscosity, $\mu \times 10^6$					Specific heat capacity, *Cp*				
Transparent cover surface	20.450	21.700	21.433	21.364	21.388	1.009	1.009	1.009	1.009	1.009
	20.690	20.855	20.840	20.700	20.675	1.009	1.009	1.009	1.009	1.009
Absorber surface										
	19.500	19.400	19.450	19.375	19.388	1.005	1.005	1.005	1.005	1.005
Chimney outlet										
	thermal conductivity, $k \times 10^2$					Density				
Transparent cover surface	3.014	3.117	3.110	3.103	3.108	1.020	0.949	0.995	0.991	0.992
	2.976	3.004	3.003	2.978	2.974	1.005	1.014	1.0139	1.006	1.004
Absorber surface										
	2.816	2.802	2.809	2.799	2.795	1.121	1.114	1.1175	1.112	1.111
Chimney outlet										

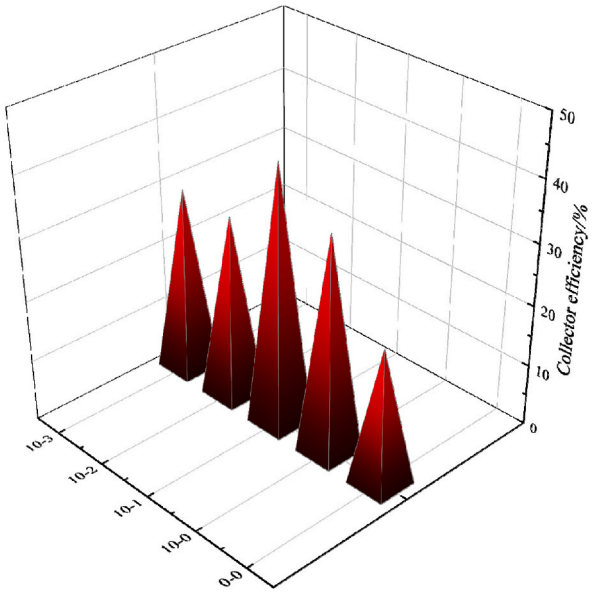
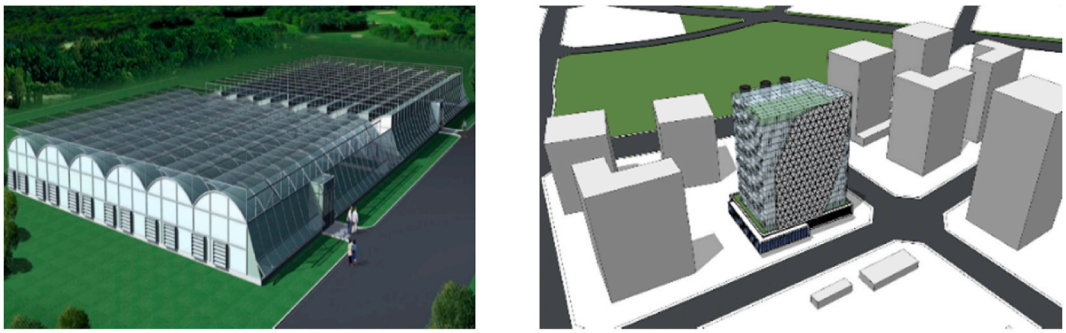


Fig. 19. Heat collection efficiency of the SCS.

electricity through a cogeneration system, meeting the power needs of the greenhouse. Incorporating the SCS into agricultural greenhouses offers several benefits. It allows for dual land use, with the top of the greenhouse used for power generation and the interior for cultivation, thus improving land use efficiency. The SCS can also create a suitable microclimate and provide optimal growing conditions for crops by regulating light and temperature, making it ideal for growing high-value-added crops. Furthermore, the heat from the SCS can be utilized in the greenhouse's temperature control system, reducing dependence on traditional energy



(a) The local facility agriculture. (b)Construction of an aerial garden based on SCS.

Fig. 20. The SCS integration with different system architectures.

sources and lowering operating costs. The key to integrating the SCS with agricultural greenhouses lies in technology integration. Various technologies, such as solar energy collection, thermal energy storage, and intelligent control systems, need to be combined into a single system for efficient energy management and environmental control. An intelligent control system can automatically adjust the operation of the SCS and optimize energy use efficiency based on the growth demands of crops and external climate conditions, see Fig. 20 (a).

4.2. Integration with sky garden

Active ventilation systems use mechanical equipment to manage airflow, which requires energy. Passive ventilation systems, on the other hand, use natural elements like wind and air convection caused by temperature differences to promote airflow, reducing the operating costs of a building over its lifetime. SCS is a type of passive ventilation technology that uses solar energy to create a thermopressor effect. This paper discusses integrating the SCS with rooftop sky gardens to achieve multiple levels of energy consumption reduction and savings. The chimney design is made of transparent or translucent materials, with the bottom connected to the building's interior to allow hot air to rise and disperse, lowering the internal temperature and allowing fresh air to enter. During nights or cloudy days, the chimney's natural convection can lower the interior temperature by opening windows or vents to expel hot air. A section of the chimney is attached to the sky garden frame, and the sizes of windows, vents, and chimney openings can be adjusted based on weather conditions and plant requirements. Integrating the SCS with rooftop sky gardens enhances the building's ecological value and raises public awareness about sustainable living and environmental protection, see Fig. 20 (b).

5. Conclusion

The paper reduces the influence of secondary flow on the SCS by improving the system structure and considering optimizing the SCS in conjunction with facility agriculture applications. This SCS experimental setup is established in Linhe District, Bayannur City, Inner Mongolia Autonomous Region. Numerical simulation studies are added with the same working conditions as the experiment. The flow field characteristics inside the SCS are analyzed, and the SCS is optimized and improved using heat collection efficiency and chimney inlet fluid velocity as objective functions. This work's results provide a theoretical basis for improving and fully characterizing the SCS structure. The conclusions are presented below:

(1) An experimental study on the SCS is carried out. The results demonstrate that the uniformity of the temperature of the SCS absorber, the distribution characteristics, and stability of the fluid temperature field at the chimney inlet, and the temperature field on the transparent cover surface is excellent when the composite absorber made up of bamboo glue board + aluminum + sand + black high-density polyethylene foam board is applied, and the transparent cover is at an inclination of 10°.
(2) The optimum inclination angle and divergence angle of the SCS suitable for the area with an analogous geographical and meteorological environment in the Linhe District of Bayannur City are obtained. The heat collection performance of the SCS with a 10° transparent cover inclination angle and a 1° chimney divergence angle is better.
(3) Optimization is carried out with heat collection efficiency and chimney inlet fluid velocity as objective functions. The results show that changing the transparent cover inclination angle and chimney dispersion angle significantly improves the heat collection efficiency, where the SCS heat collection efficiency is as high as 42.54 % when the inclination angle is 10° and the chimney dispersion angle is 1°. The chimney inlet fluid velocity of the SCS with different chimney dispersion angles at the same transparent cover inclination is different, with velocities as high as 2.090 m/s at 2°.

To address the scarcity of experimental research on solar chimney systems SCS, numerical simulation techniques are utilized. These outcomes are then used to corroborate the numerical simulations, ensuring their accuracy. This method provides a theoretical framework for enhancing the structure, choosing materials, and integrating with various energy systems within the SCS. When combined with traditional facility-based agriculture, the SCS improves the stability and efficiency of agricultural activities, reduces carbon emissions, and promotes sustainable agriculture. Additionally, combining the SCS with aerial gardens reduces energy consumption and enhances environmental benefits.

CRediT authorship contribution statement

Jing Jia: Writing – original draft, Validation, Software, Methodology, Conceptualization. **Jing Nie:** Writing – review & editing, Resources, Conceptualization. **Hao Su:** Formal analysis, Conceptualization. **Jin-Chen XU:** Formal analysis, Data curation, Conceptualization. **Xinyao Ruan:** Data curation, Conceptualization. **Wei Gao:** Formal analysis, Data curation, Conceptualization.

Declaration of competing interest

The authors declare that they have no known competing financial interests or personal relationships that could have appeared to influence the work reported in this paper.

Acknowledgments

The work presented in this paper is financially supported by grants from the Natural Science Foundation of Inner Mongolia (2021LHMS05007), Inner Mongolia Autonomous Region directly affiliated universities basic scientific research operating expenses (JY20220397), Doctoral Foundation Project of Inner Mongolia University of Technology (BS201933).

Data availability

The authors are unable or have chosen not to specify which data has been used.

References

[1] N. Pasumarthi, S.A. Sherif, Experimental and theoretical performance of a demonstration solar chimney model - Part I: mathematical model development, Int. J. Energy Res. 22 (3) (1998) 277–288.
[2] R. Balijepalli, V. Chandramohan, K. Kirankumar, Development of a small scale plant for a solar chimney power plant (SCPP): a detailed fabrication procedure, experiments and performance parameters evaluation, Renew. Energy (2020) 148247–148260.
[3] M. Ghalamchi, A. Kasaeian, M. Ghalamchi, Experimental study of geometrical and climate effects on the performance of a small solar chimney, Renew. Sustain. Energy Rev. (2015) 43425–43431.
[4] J. Nie, R. Tian, Q. Cai, et al., Optimal collector angle by test on heat collection performance of solar chimney power plant system, Trans. Chin. Soc. Agric. Eng. 34 (12) (2018) 224–229, 309.
[5] G. He, Q. Wu, Z. Li, et al., Ventilation performance of solar chimney in a test house: field measurement and validation of plume model, Build. Environ. 193 (3) (2021) 107648.
[6] T. Ming, X. Wang, R.K.D. Richter, et al., Numerical analysis on the influence of ambient crosswind on the performance of solar updraft power plant system, Renew. Sustain. Energy Rev. 16 (8) (2012) 5567–5583.
[7] H.H. Al-Kayiem, K. Sreejaya, O.A. Chikere, Experimental and numerical analysis of the influence of inlet configuration on the performance of a roof top solar chimney, Energy Build. (2018) 15989–15998.
[8] S. Golzardi, R. Mehdipour, Z. Baniamerian, How collector inlet influences the solar chimney performance: experimental assessment, J. Therm. Anal. Calorim. 146 (prepublish) (2020) 1–14.
[9] R. Mehdipour, S. Golzardi, Z. Baniamerian, Experimental justification of poor thermal and flow performance of solar chimney by an innovative indoor experimental setup, Renew. Energy 157 (prepublish) (2020) 1089–1101.
[10] A. Hassan, M. Ali, A. Waqas, Numerical investigation on the performance of solar chimney power plant by varying collector slope and chimney diverging angle, Energy 142 (2018) 411–425.
[11] A. Ayadi, Z. Driss, A. Bouabidi, et al., Experimental and numerical study of the impact of the collector roof inclination on the performance of a solar chimney power plant, Energy Build. 139 (2017) 263–276.
[12] M.H. Huang, G.X. Liu, Y.L. He, et al., Structural optimization of solar chimney power station based on genetic algorithm 55 (10) (2021) 10.
[13] N. Mehla, K. Kumar, M. Kumar, Thermal analysis of solar updraft tower by using different absorbers with convergent chimney, Environ. Dev. Sustain. 21 (3) (2018) 1251–1269.
[14] L. Zuo, L. Ding, J. Chen, et al., Comprehensive study of wind supercharged solar chimney power plant combined with seawater desalination, Sol. Energy 166 (2018) 59–70.
[15] S. Jamali, M. Yari, S.M.S. Mahmoudi, Enhanced power generation through cooling a semi-transparent PV power plant with a solar chimney, Energy Convers. Manag. 175 (2018) 227–235.
[16] M. Tingzhen, G. Haoyu, S. Tianhao, et al., Solar chimney power plant integrated with a photocatalytic reactor to remove atmospheric methane: a numerical analysis, Sol. Energy (2021) 226101–226111.
[17] M. Xie, T. Jia, Y. Dai, Hybrid photovoltaic/solar chimney power plant combined with agriculture: the transformation of a decommissioned coal-fired power plant, Renew. Energy (2022) 191.
[18] N. Jafarifar, M.M. Behzadi, M. Yaghini, The effect of strong ambient winds on the efficiency of solar updraft power towers: a numerical case study for Orkney, Renew. Energy 136 (2019) 937–944.
[19] L. Zuo, P. Dai, C. Li, et al., Study of the performance for wind supercharged solar chimney power plant affected by the chimney shadow, Renew. Energy Resour. 40 (1) (2022) 55–59.
[20] J. Wang, J. Nie, J. Jia, et al., Structural optimization to reduce the environmental crosswind negative influence on the performance of a solar chimney power plant system, Sol. Energy 241 (2022) 693–711.
[21] Y.F. Zhang, Effects of climate characteristics on crop growth in Linhe district, bayannaoer city in 2021, Jiangxi Agric. (20) (2022) 3.
[22] Q.L. Cai, J. Nie, W.W. Zhang, et al., Numerical simulation of influence of angle of fixed area heat collector on heat collection efficiency, Renew. Energy 35 (2) (2017) 5.
[23] F. Cao, L. Zhao, H. Li, et al., Performance analysis of conventional and sloped solar chimney power plants in China, Appl. Therm. Eng. 50 (1) (2013) 582–592.
[24] W.H. Chen, Y.S.H. Che, Influence of the height of heat collector on the performance of solar thermal power generation, Renew. Energy 31 (9) (2013) 4.
[25] D. Pritam, V. Chandramohan, Performance characteristics of divergent chimney solar updraft tower plant, Int. J. Energy Res. 45 (12) (2020) 17159–17174.
[26] A. Bouabidi, H. Nasraoui, A. Ayadi, et al., Numerical analysis of chimney diameter effect on the fluid flow and the heat transfer characteristics within the solar tower, Energy Sources, Part A Recovery, Util. Environ. Eff. 41 (20) (2019) 2494–2506.
[27] P. Guo, Y. Zhou, D. Zhang, et al., Numerical investigation and multi-objective thermo-economic optimization of a solar chimney power plant, Int. J. Energy Res. 45 (7) (2021) 10317–10331.
[28] T. Long, N. Zhao, W. Li, et al., Natural ventilation performance of solar chimney with and without earth-air heat exchanger during transition seasons, Energy (2022) 250.
[29] J.W. Wanf, Study on the Influence of Environmental Crosswind on Solar Chimney Power Generation System [D], Inner Mongolia University of Technology, 2022.
[30] J. Nie, J.W. Wang, J. Jia, et al., Influence of Different radiation Models on Numerical simulation of solar chimney, J. Solar Energy 43 (11) (2022) 100–105.
[31] P. Das, V.P. Chandra Mohan, Experimental studies of a laboratory scale inclined collector solar updraft tower plant with thermal energy storage system, J. Build. Eng. 41 (2021).
[32] V. Praveen, P. Das, V.P. Chandra Mohan, A novel concept of introducing a fillet at the chimney base of solar updraft tower plant and thereby improving the performance: a numerical study, Renew. Energy (2021) 179.
[33] H. Nasraoui, A. Ayadi, A. Bouabidi, et al., Influence of the collector concavity on the airflow behavior within solar chimney power plant, Int. J. Green Energy 16 (15) (2019) 1–9.
[34] F.P. Incropera, Fundamentals of Heat and Mass Transfer [J], Wiley, 2006.
[35] B. Issa, M. Hatem, O. Shinichi, et al., Applied single and hybrid solar energy techniques for building energy consumption and thermal comfort: a comprehensive review, Sol. Energy (2023) 259188–259228.